Monthly Notices
of the
ROYAL ASTRONOMICAL SOCIETY

MNRAS **483,** 3529–3544 (2019)
Advance Access publication 2018 November 16

doi:10.1093/mnras/sty3115

Physical modelling of galaxy clusters detected by the *Planck* satellite

Kamran Javid,[1,2]★ Malak Olamaie,[1,3] Yvette C. Perrott,[1] Pedro Carvalho,[1] Keith J. B. Grainge,[4] Michael P. Hobson,[1] Clare Rumsey[1] and Richard D. E. Saunders[1,2]

[1]*Astrophysics Group, Cavendish Laboratory, JJ Thomson Avenue, Cambridge CB3 0HE, UK*
[2]*Kavli Institute for Cosmology Cambridge, Madingley Road, Cambridge CB3 0HA, UK*
[3]*Imperial Centre for Inference and Cosmology (ICIC), Imperial College, Prince Concort Road, London SW7 2AZ, UK*
[4]*Jodrell Bank Centre for Astrophysics, School of Physics and Astronomy, The University of Manchester, Manchester M13 9PL, UK*

Accepted 2018 November 3. Received 2018 October 15; in original form 2018 May 4

ABSTRACT

We present a comparison of mass estimates for 54 galaxy cluster candidates from the second *Planck* catalogue (PSZ2) of Sunyaev–Zel'dovich sources. We compare the mass values obtained with data taken from the Arcminute Microkelvin Imager (AMI) radio interferometer system and from the *Planck* satellite. The former of these uses a Bayesian analysis pipeline that parametrizes a cluster in terms of its physical quantities, and models the dark matter and baryonic components of a cluster using Navarro–Frenk–White (NFW) and generalized-NFW profiles, respectively. Our mass estimates derived from *Planck* data are obtained from the results of the Bayesian detection algorithm PowellSnakes, are based on the methodology detailed in the PSZ2 paper, and produce two sets of mass estimates; one estimate is calculated directly from the angular radius θ – integrated Comptonization parameter Y posterior distributions, and the other uses a 'slicing function' to provide information on θ based on X-ray measurements and previous *Planck* mission samples. We find that for 37 of the clusters, the AMI mass estimates are lower than both values obtained from *Planck* data. However the AMI and slicing function estimates are within one combined standard deviation of each other for 31 clusters. We also generate cluster simulations based on the slicing-function mass estimates, and analyse them in the same way as we did the real AMI data. We find that inclusion in the simulations of radio-source confusion, CMB noise and measurable radio-sources causes AMI mass estimates to be systematically low.

Key words: methods: data analysis – galaxies: clusters: general – cosmology: observations.

1 INTRODUCTION

In the local Universe and out to redshifts of around two, clusters of galaxies are observed as massive gravitationally bound structures, often roughly spherical and with very dense central cores. It is over eighty years ago that it was first postulated that a galaxy cluster's mass is dominated by dark matter (Zwicky 1933; Zwicky 1937). More recently it has been shown that dark matter contributes ≈90 per cent of the cluster mass (see e.g. Vikhlinin et al. 2006; Komatsu et al. 2011). Stars, gas, and dust in galaxies, as well as a hot ionized intracluster medium (ICM), make up the rest of the mass in a cluster, with the latter being the most massive baryonic component. The galaxies emit in the optical and infrared wavebands, whilst the ICM emits in X-ray via thermal bremsstrahlung and also interacts with cosmic microwave background (CMB) photons via inverse Compton scattering. This last effect is what is known as the Sunyaev–Zel'dovich (SZ) effect (Sunyaev & Zeldovich 1970). It is this effect which is detected by the *Planck* satellite and the Arcminute Microkelvin Imager (AMI) radio interferometer system, which are the telescopes featured in this analysis. The clusters detected by *Planck* form the basis of the sample considered in this work. Perrott et al. (2015; from here on YP15) present the results of the AMI follow-up of *Planck* clusters – this follow-up is analysed using the 'observational model' (Olamaie et al. 2012), which parametrizes a cluster in terms of its integrated Comptonization parameter Y and angular scale θ. YP15 find that these AMI estimates for Y are consistently lower than the values obtained from *Planck* data, and conclude that this may indicate that the cluster pressure profiles are deviating from the 'universal' one. Here, we try to overcome this by considering a model which uses redshift information to break this degeneracy. We use a physical model largely based on the one described in Olamaie, Hobson & Grainge (2012; from here on MO12), with data obtained from AMI of clusters detected by *Planck* (including ones which were detected after the analysis in YP15 was carried out). We also consider the cluster mass estimates

★ E-mail: kj316@mrao.cam.ac.uk

given in the *Planck* cluster catalogue Planck Collaboration XXVII (2016) and compare them with the values obtained using AMI data. Furthermore we use the *Planck* cluster catalogue mass estimates as inputs to simulations which are then analysed in the same way as real AMI observations.

In Section 2, we give an overview of the *Planck* mission and AMI in the context of *Planck* observed clusters. In Section 3, we review how the physical modelling process works with data obtained from AMI, and we summarize the methodology used to obtain the mass estimates given in Planck Collaboration XXVII (2016). Sections 4 and 5 present the results of our analysis, including simulated AMI data which used mass estimates obtained from *Planck* data as inputs.

A 'concordance' flat ΛCDM cosmology is assumed: $\Omega_{\rm M} = 0.3$, $\Omega_\Lambda = 0.7$, $\Omega_{\rm R} = 0$, $\Omega_{\rm K} = 0$, $h = 0.7$, $H_0 = 100h{\rm kms}^{-1}$ Mpc^{-1}, $\sigma_8 = 0.8$, $w_0 = -1$, and $w_{\rm a} = 0$. The first four parameters correspond to the (dark + baryonic) matter, the cosmological constant, the radiation, and the curvature densities, respectively. h is the dimensionless Hubble parameter, while H_0 is the Hubble parameter now and σ_8 is the power spectrum normalization on the scale of 8 h^{-1} Mpc now. w_0 and $w_{\rm a}$ are the equation-of-state parameters of the Chevallier–Polarski–Linder parametrization (Chevallier & Polarski 2001).

2 *PLANCK* AND AMI TELESCOPES, AND THE CLUSTER SAMPLE

2.1 *Planck* mission

The combination of the *Planck* satellite's low-frequency and high-frequency instruments provide nine frequency channels in the range 37–857 GHz. Of particular importance for the work described here are the *Planck* cluster-catalogues [see Planck Collaboration XXIX (2014), Planck Collaboration XXXII (2015), and Planck Collaboration XXVII (2016) for papers relating to catalogues PSZ1, PSZ1.2, and PSZ2, respectively, where 'PSZX' refers to the Xth *Planck* SZ catalogue]. These provide, for example, cluster candidate positions, redshift (z) values, integrated Comptonization parameter values, and mass (M) estimates. PSZ2 is the most recent all-sky *Planck* cluster catalogue, and is the one which we refer to in this paper unless stated otherwise.

2.2 PSZ2 redshift values

Catalogue z values are measured in the optical/infrared or X-ray, with major input from the Sloan Digital Sky Survey (York et al. 2000). A number of cluster catalogues have been extracted from these data (see e.g. Hao et al. 2010; Wen, Han & Liu 2012; Rykoff et al. 2014), providing estimates of both spectroscopic and photometric z values, the reliability of the latter values falls as z increases. In the X-ray part of the spectrum, the Meta-Catalogue of X-ray detected Clusters of galaxies, or MCXC (Piffaretti et al. 2011) has a substantial number of matches with the *Planck*-catalogue clusters. The MCXC is from the available catalogues based on the ROSAT All-Sky Survey (Voges et al. 1999) as well as serendipitous X-ray catalogues (see e.g. Gioia et al. 1990). MCXC contains only clusters with measured z, but does not state the redshift type or source. Further sources of *Planck* catalogue clusters candidate zs are the Russian–Turkish Telescope (Planck Collaboration XXVI 2015) and the ENO telescopes in the Canary Islands (Planck Collaboration XXXVI 2016); for each z these state whether it was obtained photometrically or spectroscopically.

Table 1. Summary of AMI characteristics.

	SA	LA
Antenna diameter	3.7 m	12.8 m
Number of antennas	10	8
Baseline lengths (current)	5–20 m	18–110 m
Primary beam FWHM (at 15.7 GHz)	20.1 arcmin	5.5 arcmin
Typical synthesized beam FWHM	3 arcmin	30 arcsec
Flux sensitivity	30 mJy s$^{1/2}$	3 mJy s$^{1/2}$

2.3 AMI

AMI is an interferometer system near Cambridge, UK, designed for SZ studies (see e.g. Zwart et al. 2008). It consists of two arrays: the Small Array (SA), optimized to couple to SZ signal, with an angular resolution of ≈3 arcmin and sensitivity to structures up to ≈10 arcmin in scale; and the Large Array (LA), with angular resolution of ≈30 arcsec, which is largely insensitive to SZ, and is used to characterize and subtract confusing radio-sources. Both arrays operate at a central frequency of ≈15.7 GHz, and at the time the AMI data for this paper were taken, with a bandwidth of ≈4.3 GHz, divided into six channels. A summary of AMI's characteristics is given in Table 1. Note that AMI has recently received a new digital correlator (Hickish et al. 2018), but all real data used in this work were obtained by the system with its old analogue correlator.

Our pointing strategy for each cluster was as follows. Clusters were observed using a single pointing centre on the SA, which has a primary beam of size ≈20 arcmin FWHM, to noise levels of $\lesssim$120 μJy beam^{-1}. To cover the same area with the LA, which has a primary beam of size ≈6 arcmin FWHM, the cluster field was observed as a 61-point hexagonal raster. The noise level of the raster was $\lesssim$100 μJy beam^{-1} in the central 19 pointings, and slightly higher in the outer regions. The observations for a given cluster field were carried out simultaneously on both arrays, and the average observation time per cluster was ≈30 h. The observations were carried out between 2013 and 2015, and so they began before PSZ2 was published. This means that the AMI pointing centre coordinates in general were not the same as those published in the final *Planck* catalogue which was released in 2015. This is discussed in the context of the cluster centre offset parameters in Section 3.2.1.

Data from both arrays were flagged for interference and calibrated using the AMI in-house software package REDUCE. Flux calibration was applied using contemporaneous observations of the primary calibration sources 3C 286, 3C 48, and 3C 147. The assumed flux densities for 3C 286 were converted from Very Large Array total-intensity measurements (Perley & Butler 2013) and are consistent with Rudy et al. (1987). The assumed flux densities for 3C 48 and 3C 147 were based on long-term monitoring with the SA using 3C 286 for flux calibration. Phase calibration was applied using interleaved observations of a nearby bright source selected from the Very Long Baseline Array Calibrator survey (Petrov et al. 2008); in the case of the LA, a secondary amplitude calibration was also applied using observations of the phase calibration source on the SA.

2.4 Selection of the cluster sample

PSZ2 contains 1653 cluster candidates detected in the all-sky 29 month mission. The initial cluster selection criteria for AMI closely resembles that described in YP15, with a few modifications as follows:

Table 2. Minimum and maximum values for a selection of parameters taken from PSZ2 for the AMI sample of 199 clusters.

Parameter	Minimum value	Maximum value
Declination	20°.31	86°.24
z	0.045	0.83
S/N	4.50	28.40
$M_{\rm SZ}$ ($\times 10^{14}$ M$_\odot$)	1.83	10.80

(i) The lower z limit $z \leq 0.100$ was relaxed here, to see how well AMI data can constrain the the physical model parameters at low redshift. However it is important to realize that the sample at $z \leq 0.100$ were not observed specifically for the purpose of this work, but were part of other observation projects.

(ii) The *Planck* signal-to-noise ratio (S/N) lower bound was reduced to 4.5.

(iii) The automatic radio-source environment rejection remained the same. However the manual rejection was done on a map-by-map basis – see Section 4.

(iv) Note that the observation declination limits $20^\circ < \delta < 87^\circ$ were kept.

This led to an initial sample size of 199 clusters, The maximum and minimum values of some key parameters for this sample from the *Planck* catalogue are given in Table 2. Note that $M_{\rm SZ}$ is taken in PSZ2 as the hydrostatic equilibrium mass $M(r_{500})$, assuming the best-fitting Y–M relation (see Section 3.3.2).

3 AMI DATA ANALYSIS AND PSZ2 SCALING RELATIONS METHODOLOGY

Our AMI Bayesian data analysis pipeline, MCADAM closely resembles the one described in Feroz et al. (2009; FF09 from here on). In this section the key aspects of the analysis are summarized, and also we note modifications specific to the work of this paper.

3.1 A physical model for AMI data

In the implementation of McAdam used here, we in large employed the model of MO12 to derive physical properties of a galaxy cluster (i.e. mass, pressure, density, radius, and temperature values) from the data obtained from an SZ-detecting interferometer plus z-information. The model assumes an Navarro–Frenk–White (NFW) profile (Navarro, Frenk & White 1995) for the dark matter density as a function of cluster radius r,

$$\rho_{\rm dm}(r) = \frac{\rho_{\rm s}}{\left(\frac{r}{r_{\rm s}}\right)\left(1+\frac{r}{r_{\rm s}}\right)^2}, \quad (1)$$

where $\rho_{\rm s}$ is an overall density normalization coefficient and $r_{\rm s}$ is a characteristic radius defined by $r_{\rm s} \equiv r_{200}/c_{200}$ and is the radius at which the logarithmic slope of the profile $\mathrm{d}\ln\rho(r)/\mathrm{d}\ln r$ is -2. r_{200} is the radius at which the *mean* cluster density is $200 \times \rho_{\rm crit}(z)$. $\rho_{\rm crit}(z)$ is the critical density of the Universe at the cluster z which is given by $\rho_{\rm crit}(z) = 3H(z)^2/8\pi G$, where $H(z)$ is the Hubble parameter (at the cluster redshift) and G is Newton's constant. c_{200} is the concentration parameter at this radius. Following Olamaie, Hobson & Grainge (2013), we calculate c_{200} for an NFW dark matter density profile taken from the expression in Corless, King & Clowe (2009)

$$c_{200} = \frac{5.26}{1+z}\left(\frac{M(r_{200})}{10^{14}h^{-1}M_{\rm Sun}}\right)^{-0.1}. \quad (2)$$

The $1/(1+z)$ factor comes from Wechsler et al. (2001) and is obtained from N-body simulated dark matter haloes between $z = 0$ and $z = 7$. The remainder of the relation was derived in Neto et al. (2007) by fitting a power law for c_{200} to N-body simulated cluster data. Note that the sample used in Neto et al. (2007) was assumed to contain clusters that are relaxed. In equation (2) $M(r_{200})$ is the mass enclosed at radius r_{200}. Thus for given values of z and $M(r_{200})$ (which are input parameters to the model, see Section 3.2.1), c_{200} can be calculated. Furthermore if we take $M(r_{200}) = 200 \times \frac{4\pi}{3}\rho_{\rm crit}(z)r_{200}^3$ then we can also calculate r_{200} and so $r_{\rm s}$.

Following Nagai, Kravtsov & Vikhlinin (2007), the generalized NFW (GNFW) model is used to parametrize the electron pressure as a function of radius from the cluster centre

$$P_{\rm e}(r) = \frac{P_{\rm ei}}{\left(\frac{r}{r_{\rm p}}\right)^c\left(1+\left(\frac{r}{r_{\rm p}}\right)^a\right)^{(b-c)/a}}, \quad (3)$$

where $P_{\rm ei}$ is an overall pressure normalization factor and $r_{\rm p}$ is another characteristic radius, defined by $r_{\rm p} \equiv r_{500}/c_{500}$ (r_{500} is the radius at which the cluster density is $500 \times \rho_{\rm crit}(z)$]. The parameters a, b, and c describe the slope of the pressure profile at $r/r_{\rm p} \approx 1$, $r/r_{\rm p} \gg 1$, and $r/r_{\rm p} \ll 1$, respectively. For values $r/r_{\rm p} \ll 1$ the logarithmic slope ($\mathrm{d}\ln P_{\rm e}(r)/\mathrm{d}\ln r$) converges to $-c$. For values $r/r_{\rm p} \gg 1$ the logarithmic slope converges to $-b$. The value of a dictates how quickly (in terms of r) the slope switches between these two values, and in the limit that a tends to zero, the logarithmic slope is $-(b+c)/2$ for all r. Consistent with many of the *Planck* follow-up papers (see e.g. Planck Collaboration VIII 2011) and with MO12 the slope parameters are taken to be $a = 1.0620$, $b = 5.4807$, and $c = 0.3292$. These 'universal' values are from Arnaud et al. (2010) and are the GNFW slope parameters derived for the standard self-similar case using scaling relations from a REXCESS subsample (of 20 well-studied low-z clusters observed with *XMM–Newton*), as described in Appendix B of the paper (Böhringer et al. 2007). We also use the Arnaud et al. value for the concentration parameter $c_{500} \equiv r_{500}/r_{\rm p}$ of 1.156. We note however that in YP15 using simulations it was shown that the disagreement between *Planck* and AMI parameter estimates may indicate pressure profiles deviating from the 'universal' profile. For any model it is important to know the underlying assumptions which allow it to be valid. The four relevant assumptions in MO12 are following:

(i) The cluster is spherically symmetric.

(ii) The cluster is in hydrostatic equilibrium up to radius r_{200}. This means at any radius up to r_{200} the outward pushing pressure force created by the pressure differential at that point must be equal to the gravitational binding force due to the mass enclosed within that radius (Bahcall & Sarazin 1977, see equation 4 of MO12).

(iii) The gas mass fraction $f_{\rm gas}(r)$ is much less than unity up to radius r_{200}, so that the total mass is $M(r_{200}) \approx M_{\rm dm}(r_{200})$. Consequently the total mass out to r_{200} is given by the integral of the dark matter density along the radius of the cluster (equation 5 of MO12).

(iv) The cluster gas is assumed to be an ideal gas, so that its temperature can be trivially represented in terms of its pressure (equations 13 and 14 of MO12).

The calculation steps used for the present paper are as described in MO12 except for one modification. Previously, the mapping from r_{200} to r_{500} was a constant factor $\frac{2}{3}$ which was derived by solving

the equation

$$\left(\frac{r_s}{r_{500}}\right)^3\left[\ln\left(1+\frac{r_{500}}{r_s}\right)-\left(1+\frac{r_s}{r_{500}}\right)^{-1}\right]$$
$$=\frac{5}{2}\left(\frac{r_s}{r_{200}}\right)^3\times\left[\ln\left(1+\frac{r_{200}}{r_s}\right)-\left(1+\frac{r_s}{r_{200}}\right)^{-1}\right] \quad (4)$$

for a range of values of $M(r_{200})$ and z. However, following Hu & Kravtsov (2003), there is an analytic mapping from r_{200} to r_{500}. Consider the equation

$$g(r_s/r_{500})=\frac{5}{2}g(r_s/r_{200}), \quad (5)$$

where

$$g(x)=x^3[\ln(1+x^{-1})-(1+x)^{-1}]. \quad (6)$$

Equation (5) requires that $g(r_s/r_{500})$ be inverted so that

$$\frac{r_s}{r_{500}}=x\left(g_{500}=\frac{5}{2}f(r_s/r_{200})\right), \quad (7)$$

where

$$x(g_{500})=\left[a_1 g_{500}^{2p}+\frac{9}{16}\right]^{-1/2}+2g_{500}. \quad (8)$$

Here $p=a_2+a_3\ln g_{500}+a_4(\ln g_{500})^2$, and the four-fitting parameters correspond to $a_1=0.5116$, $a_2=-0.4283$, $a_3=-3.13\times10^{-3}$, and $a_4=-3.52\times10^{-5}$. This gives a fit to better than 0.3 per cent accuracy for $0<c_{200}<20$ and is exact in the limit that $c_{200}\to0$.

3.2 Bayesian parameter estimation

Given a model $\mathcal{M}$ and a data vector $\mathcal{D}$, one can obtain model parameters (also known as input or sampling parameters) $\boldsymbol{\Theta}$ conditioned on $\mathcal{M}$ and $\mathcal{D}$ using Bayes' theorem:

$$Pr(\boldsymbol{\Theta}|\mathcal{D},\mathcal{M})=\frac{Pr(\mathcal{D}|\boldsymbol{\Theta},\mathcal{M})\,Pr(\boldsymbol{\Theta}|\mathcal{M})}{Pr(\mathcal{D}|\mathcal{M})}, \quad (9)$$

where $Pr(\boldsymbol{\Theta}|\mathcal{D},\mathcal{M})\equiv\mathcal{P}(\boldsymbol{\Theta})$ is the posterior distribution of the model parameter set, $Pr(\mathcal{D}|\boldsymbol{\Theta},\mathcal{M})\equiv\mathcal{L}(\boldsymbol{\Theta})$ is the likelihood function for the data, $Pr(\boldsymbol{\Theta}|\mathcal{M})\equiv\pi(\boldsymbol{\Theta})$ is the prior probability distribution for the model parameter set, and $Pr(\mathcal{D}|\mathcal{M})\equiv\mathcal{Z}(\mathcal{D})$ is the Bayesian evidence of the data given a model $\mathcal{M}$. The evidence can be interpreted as the factor required to normalize the posterior over the model parameter space:

$$\mathcal{Z}(\mathcal{D})=\int\mathcal{L}(\boldsymbol{\Theta})\pi(\boldsymbol{\Theta})\,\mathrm{d}\boldsymbol{\Theta}, \quad (10)$$

where the integral is carried out over the N-dimensional parameter space. Although $\mathcal{Z}(\mathcal{D})$ is not important in the context of parameter estimation, it is central to the way that the posterior distributions are determined using the nested sampling algorithm MULTINEST (Feroz, Hobson & Bridges 2009). MULTINEST is a Monte Carlo algorithm which makes use of a transformation of the N-dimensional evidence integral into a much easier to evaluate one-dimensional integral, and generates samples from the posterior distribution $\mathcal{P}(\boldsymbol{\Theta})$ as a by-product. The input parameters can be split into two subsets (which are assumed to be independent of one another): cluster parameters $\boldsymbol{\Theta}_{\rm cl}$ and radio-source or 'nuisance' parameters $\boldsymbol{\Theta}_{\rm rs}$.

Table 3. Cluster parameter prior distributions. δ denotes a Dirac delta function, $\mathcal{U}$ is a uniform distribution, and $\mathcal{N}$ is a normal distribution (parametrized by its mean and standard deviation).

Parameter	Prior distribution
x_c	$\mathcal{N}(0'', 60'')$
y_c	$\mathcal{N}(0'', 60'')$
z	$\delta(z_{\rm Planck})$
$M(r_{200})$	$\mathcal{U}[\log(0.5\times10^{14}\,{\rm M}_\odot), \log(50\times10^{14}\,{\rm M}_\odot)]$
$f_{\rm gas}(r_{200})$	$\mathcal{N}(0.13, 0.02)$

3.2.1 Cluster parameter prior distributions

Following FF09, the cluster parameters are assumed to be independent of one another, so that

$$\pi(\boldsymbol{\Theta}_{\rm cl})=\pi(M(r_{200}))\pi(f_{\rm gas}(r_{200}))\pi(z)\pi(x_c)\pi(y_c). \quad (11)$$

x_c and y_c are the cluster centre offsets from the SA pointing centre, measured in arcseconds. The prior distributions assigned to the cluster parameters are the same as the ones used in Olamaie et al. (2013), but with an alteration to the mass limits. Upon running MCADAM on data from a few of the *Planck* clusters, it was found that the posterior distributions of $M(r_{200})$ were hitting the lower bound 1×10^{14} M$_\odot$ used in Olamaie et al. (2013). Hence for this analysis the lower limit on $M(r_{200})$ was decreased. Table 3 lists the type of prior used for each cluster parameter and the probability distribution parameters. Values for $z_{\rm Planck}$ were taken from the PSZ2 catalogue.

3.2.2 Measured radio-source parameter prior distributions

Each radio-source recognized and measured by the LA can also be modelled in the analysis. Following FF09, each source can be parametrized by four variables: its position on the sky ($x_{\rm rs}$, $y_{\rm rs}$), its measured flux density $S_{\rm rs}$, and its spectral index $\alpha_{\rm rs}$. The latter of these quantities describes how the flux density of a radiating object depends on the frequency of the radiation. Assuming these are independent, then for source i

$$\pi(\boldsymbol{\Theta}_{{\rm rs},i})=\pi(x_{{\rm rs},i})\pi(y_{{\rm rs},i})\pi(S_{{\rm rs},i})\pi(\alpha_{{\rm rs},i}). \quad (12)$$

Delta functions are applied to the distributions on $x_{\rm rs}$ and $y_{\rm rs}$, due to the LA's ability to measure spatial positions to high accuracy: $\pi(x_{\rm rs})=\delta(x_{\rm rs,\,LA})$, $\pi(y_{\rm rs})=\delta(y_{\rm rs,\,LA})$. Delta priors were also set on $S_{\rm rs}$ and $\alpha_{\rm rs}$ (centred on the values measured by the LA), if the measured $S_{\rm rs}$ was less than four times the instrumental noise associated with the observation, and the source was more than 5 arcminutes away from the SA pointing centre: $\pi(S_{\rm rs})=\delta(S_{\rm rs,\,LA})$, $\pi(\alpha_{\rm rs})=\delta(\alpha_{\rm rs,\,LA})$. Otherwise, a Gaussian prior was set on $S_{\rm rs}$ centred at the LA measured value with a standard deviation equal to 40 per cent of the measured value ($\sigma_{\rm rs}=0.4\times S_{\rm rs,\,LA}$): $\pi(S_{\rm rs})\sim\mathcal{N}(S_{\rm rs,\,LA},\sigma_{\rm rs})$. The spectral index $\alpha_{\rm rs}$ was modelled using the empirical distribution determined in Waldram et al. (2007): $\pi(\alpha_{\rm rs})=\mathcal{W}(\alpha_{\rm rs})$.

3.2.3 Likelihood function

Following Hobson & Maisinger (2002) and FF09, the likelihood function is given by

$$\mathcal{L}(\boldsymbol{\Theta})=\frac{1}{Z_D}\mathrm{e}^{-\frac{1}{2}\chi^2}. \quad (13)$$

Here χ^2 is a measure of the goodness-of-fit between the real and modelled data and can be expressed as

$$\chi^2 = \sum_{\nu,\nu'} (\boldsymbol{d}_\nu - \boldsymbol{d}^{\rm p}_\nu(\boldsymbol{\Theta}))^{\rm T} \mathbf{C}^{-1}_{\nu,\nu'} (\boldsymbol{d}_{\nu'} - \boldsymbol{d}^{\rm p}_{\nu'}(\boldsymbol{\Theta})). \quad (14)$$

In this expression $\boldsymbol{d}_\nu$ are the real data observed by AMI at frequency ν, and $\boldsymbol{d}^{\rm p}_\nu(\boldsymbol{\Theta})$ are the predicted data generated by the model also at frequency ν. AMI data are measured in six neighbouring frequency channels as described in Zwart et al. (2008). To generate the predicted data points, values are sampled from $\pi(\boldsymbol{\Theta})$ which are used in the calculations outlined in MO12 and Olamaie et al. (2013) to generate a pressure profile for the cluster which can be used to replicate the SZ signal measured by an interferometer as detailed in sections 4 and 5 of FF09. $\mathbf{C}_{\nu,\nu'} \equiv \mathbf{C}^{\rm ins}_{\nu,\nu'} + \mathbf{C}^{\rm CMB}_{\nu,\nu'} + \mathbf{C}^{\rm conf}_{\nu,\nu'}$ is the theoretical covariance matrix, which includes instrumental, primordial CMB, and source confusion noise as described in FF09 and Hobson & Maisinger (2002). Source confusion noise allows for the remaining radio-sources with flux densities less than some flux limit $S_{\rm lim}$, that cannot be measured accurately by the LA. The instrumental noise is actually measured during the observation and so does not need to be predicted. Referring back to equation (13), Z_D is a normalization constant given by $(2\pi)^{D/2}|\mathbf{C}|^{1/2}$, where D is the length of $\boldsymbol{d}$ (the vector of data from all frequencies).

3.3 PSZ2 methodology for deriving cluster mass estimates

For comparison with the mass values obtained with AMI data, we look at the PSZ2 mass estimates obtained from *Planck* data and the requisite scaling relations. The mass values published in PSZ2 are derived from data from one of three detection algorithms: MMF1, MMF3 {both of which are extensions of the matched multifilter algorithm suitable for SZ studies [MMF, see Haehnelt & Tegmark (1996), Herranz et al. (2002), and Melin, Bartlett & Delabrouille (2006)], over the whole sky} and PowellSnakes (PwS; Carvalho et al. 2012). The former two rely on multifrequency matched-filter detection methods, whilst PwS is a fully Bayesian method. Since the PwS methodology most closely matches the Bayesian analysis pipeline used for AMI data, we focus on the cluster parameter values from PwS.

The observable quantity measured by *Planck* is the integrated Comptonization parameter Y. As described in Section 5 of the PSZ2 paper (Planck Collaboration XXVII 2016), for each cluster candidate a two-dimensional posterior for the integrated Comptonization parameter within the radius $5r_{500}$, $Y(5r_{500})$ and the angular scale radius of the GNFW pressure, $\theta_{\rm p}$ ($=r_{\rm p}/D_A$). The values for $Y(5r_{500})$ published in PSZ2 are obtained by marginalizing over $\theta_{\rm p}$ and then taking the expected value of $Y(5r_{500})$. We will refer to this value as $Y_{\rm marg}(5r_{500})$. As described in sections 5.2 and 5.3 of Planck Collaboration XXVII (2016), this 'blind' measurement of the integrated Comptonization parameter may not be reliable when the underlying cluster pressure distribution deviates from that given by the GNFW model. To overcome this, a function relating $Y(5r_{500})$ and $\theta_{\rm p}$ is derived in an attempt to provide prior information on the angular scale of the cluster based on X-ray measurements and earlier *Planck* mission samples. We refer to this function as the slicing function.

3.3.1 *Derivation of the slicing function*

The scaling relations considered here are given in Planck Collaboration XX (2014). Of particular importance to deriving the slicing function, are the $Y(r_{500})$–$M(r_{500})$ and θ_{500}–$M(r_{500})$ relations. The first of these is given by

$$E(z)^{-2/3}\left[\frac{D_A^2 Y(r_{500})}{10^{-4}\,{\rm Mpc}^2}\right] = 10^{-0.19\pm0.02}\left[\frac{(1-b)M(r_{500})}{6\times10^{14}M_\odot}\right]^{1.79\pm0.08}, \quad (15)$$

where $E(z) = \sqrt{\Omega_{\rm M}(1+z)^3+\Omega_\Lambda}$ and is equal to the ratio of the Hubble parameter evaluated at redshift z to its value now for a flat ΛCDM Universe. The factor in the exponent $-2/3$ arises from the scaling relations between mass, temperature and Comptonization parameter given by equations (1)–(5) in Kravtsov, Vikhlinin & Nagai (2006). $(1-b)$ represents a bias factor, which is assumed in Planck Collaboration XX (2014) to contain four possible observational biases of departure from hydrostatic equilibrium, absolute instrument calibration, temperature inhomogeneities, and residual selection bias. Its value is calculated to be $(1-b) = 0.80^{+0.02}_{-0.01}$ from numerical simulations as described in appendix A4 of Planck Collaboration XX (2014). Equation (15) uses the fitting parameters from the relation between $Y_{\rm X}(r_{500})$ [the X-ray 'analogue' of the integrated Comptonization parameter see e.g. Kravtsov et al. (2006)], $Y_{\rm X}(r_{500}) \equiv M_{\rm g}(r_{500})T_X$, where $M_{\rm g}$ is the cluster gas mass within r_{500} and T_X is the spectroscopic temperature in the range $[0.15, 0.75]r_{500}$) and the X-ray hydrostatic mass, $M_{\rm HE}(r_{500})$ (which is equal to $(1-b)M(r_{500})$), established for 20 local *relaxed* clusters by Arnaud et al. (2010) to give the relation between the X-ray mass proxy $M_{Y_X}(r_{500})$ and $M(r_{500})$. Finally, the fitting parameters for the $Y(r_{500})$–$M_{Y_X}(r_{500})$ relation are obtained empirically from a 71-cluster sample consisting of SZ data from the *Planck* Early SZ clusters (Planck Collaboration XI 2011), of *Planck*-detected LoCuSS clusters (Planck Collaboration III 2013) and from the *XMM–Newton* validation programme (Planck Collaboration IX 2011), all with X-ray data taken from *XMM–Newton* observations (Mehrtens et al. 2012; Willis et al. 2013).

The θ_{500}–$M(r_{500})$ relation is based on the equation $M(r_{500}) = 500\times\frac{4\pi}{3}\rho_{\rm crit}(z)r^3_{500}$ and is given by

$$\theta_{500} = 6.997\left[\frac{h}{0.7}\right]^{-2/3}\left[\frac{(1-b)M_{500}}{3\times10^{14}M_{\rm Sun}}\right]^{1/3}E(z)^{-2/3}\left[\frac{D_A}{500{\rm Mpc}}\right]. \quad (16)$$

Equations (15) and (16) can be solved for $(1-b)M(r_{500})$ and equated to give $Y(r_{500})$ as a function of θ_{500}

$$Y(r_{500}) = \left[\frac{\theta_{500}}{6.997}\right]^{5.4\pm0.2}\left[\frac{h}{0.7}\right]^{3.60\pm0.13}\left[\frac{E(z)^{4.26\pm0.13}D_A^{3.4\pm0.2}}{10^{19.29\pm0.54}{\rm Mpc}^{3.4\pm0.2}}\right], \quad (17)$$

where $Y(r_{500})$ is in sr. Assuming a GNFW pressure profile, $Y(r_{500})$ can be converted to the corresponding value of $Y(5r_{500})$, through the relation

$$\frac{Y(r_{500})}{Y(5r_{500})} = \frac{B\left(\frac{(c_{500})^a}{1+(c_{500})^a};\frac{3-c}{a},\frac{b-3}{a}\right)}{B\left(\frac{(5c_{500})^a}{1+(5c_{500})^a};\frac{3-c}{a},\frac{b-3}{a}\right)}, \quad (18)$$

where $B(x;y,z) = \int_0^x t^{y-1}(1-t)^{z-1}{\rm d}t$ is the incomplete beta function. For the GNFW parameter values used in equation (3), equation (18) gives a value of 0.55. Similarly, θ_{500} can be related to $\theta_{\rm p}$ through the relation $\theta_{\rm p} = \theta_{500}/c_{500}$.

3.3.2 *Mass estimates*

For a given cluster, the resulting $Y(5r_{500})$ function is used to 'slice' the posterior, and the value where the function intersects the pos-

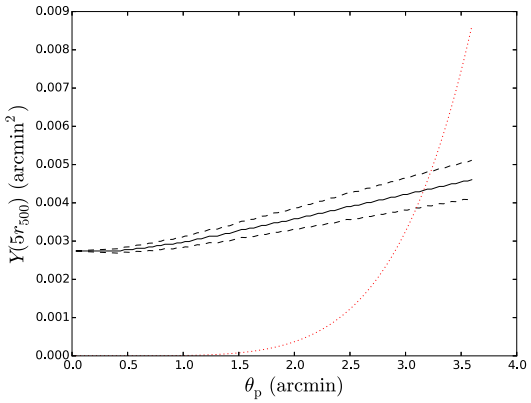

Figure 1. Example of the posterior slicing methodology for cluster PSZ2 G228.16+75.20. The black solid curve represents the 'ridge' [i.e. the most probable value of $Y(5r_{500})$ for each θ_p] of the posterior. The upper dashed curve represents the upper boundaries of the 68 per cent maximum likelihood confidence interval on $Y(5r_{500})$ for each value of θ_p, and the lower dashed curve corresponds to the lower boundaries. The red dotted curve is the slicing function.

terior 'ridge' is taken to be the most reliable estimate of $Y(5r_{500})$, given the external information. The posterior ridge (see Fig. 1) is defined to be the value of $Y(5r_{500})$ which gives the highest probability density for a given θ_p. The error estimates are obtained by considering where the slicing function intersects with the ridges defined by the 68 per cent maximum likelihood confidence intervals for $Y(5r_{500})$ at each θ_p. $Y(5r_{500})$ is then converted to $Y(r_{500})$ using the the reciprocal of the value given by equation (18), and this is used to derive a value for $M(r_{500})$ using equation (15), but with the $(1 - b)$ term excluded. The bias term is not included in the $M(r_{500})$ calculation because it has already been accounted for in the slicing function. Note that this value of $M(r_{500})$ is what is referred to as M_{SZ} in PSZ2.

4 AMI AND PSZ2 MASS ESTIMATES

First we describe how we arrived at a final sample of clusters for which the AMI mass estimates are compared with those derived from *Planck* data.

4.1 Final cluster sample

4.1.1 Well-constrained posterior sample

MCADAM was used on data from the initial sample of 199 clusters. MULTINEST failed to produce posterior distributions for two clusters. These clusters were surrounded by high flux, extended radio-sources. Of the 197 clusters for which posterior distributions were produced, 73 clusters show good constraints (adjudged by physical inspection) on the sampling parameters $M(r_{200})$, $f_{gas}(r_{200})$, x_c, and y_c; with zs ranging from 0.089 to 0.83.

We illustrate a 'well constrained' posterior distribution (for cluster PSZ2 G184.68+28.91) in the first half of Fig. 2, plotted using GETDIST.[1] In contrast the second half of Fig. 2 is an example of a cluster (PSZ2 G121.77+51.75) which shows poor constraints on mass as the posterior distribution is peaked at the lower boundary of the mass sampling range (5×10^{13} M$_\odot$) which could not be classed as a detection within our mass prior range. We also note that in the latter case the mass posterior largely resembles the log uniform prior distribution.

4.1.2 Moderate radio-source environment sample

For the 197 cluster sample, AMI data maps were produced using the software package AIPS[2] using the automated CLEAN procedure with a limit determined using IMEAN. Source-finding was carried out at a four σ level on the LA continuum map, as described in Davies et al. (2011) and Franzen et al. (2011). For each cluster both a non-source-subtracted and a source-subtracted map was produced. The values used to subtract the sources from the maps were the mean values of the one-dimensional marginalized posterior distributions of the sources' position, flux, and spectral index produced by MCADAM. Maps of the 73 cluster sample were inspected in detail. It was found that for seven of these clusters, even though the posterior distributions were well constrained, that the radio-source and primordial CMB contamination could bias the cluster parameter estimates in an unpredictable way. In these cases it was found that the subtracted maps contained residual flux close to the cluster centre, from either radio-sources (some of which were extended), radio-frequency interference, or CMB. PSZ2 G125.37−08.67 is an example of one of these clusters and its non-source-subtracted and source-subtracted maps are shown in Fig. 3. We thus arrived at a 66 cluster sample.

4.1.3 Well-defined cluster-centre sample

The posteriors of x_c and y_c give the position of the modelled cluster centre relative to the actual SA pointing centre used for the observation. For seven of the 66 cluster sample, it was found that the mean posterior values of x_c and y_c changed dramatically between different runs of MCADAM (on the same cluster data), by up to 70 arcsec in either direction, leading to differences in mass estimates of up to 70 per cent. The estimates for these clusters are not reliable, since the model was creating a completely different cluster between runs, and so these clusters were excluded leaving a 59 cluster sample. For the remaining clusters, the change in $M(r_{200})$ between runs was much smaller than the standard deviation of the corresponding posterior distributions. Fig. 4 shows the subtracted map for PSZ2 G183.90+42.99, which we consider to be an example of a cluster with an ill-defined centre. The map shows three flux decrement peaks close to the cluster centre. Movement of the centre between these peaks with the current source environment modelling would lead to a change in the size of the predicted cluster, and consequently different mass estimates each time.

4.1.4 PwS detected cluster sample

For five of the 59 cluster sample, the data available on the *Planck* website[3] did not contain a detection using the PwS algorithm, and so no mass estimates based on PwS data could be calculated. Hence the final sample size for which we present the mass estimates from both AMI and *Planck* data is 54.

It is important to realize that selection biases are introduced in reducing the sample size from 199 to 54. In particular, selecting

[1] http://getdist.readthedocs.io/en/latest/.

[2] http://aips.nrao.edu/.

[3] https://pla.esac.esa.int/pla/catalogues.

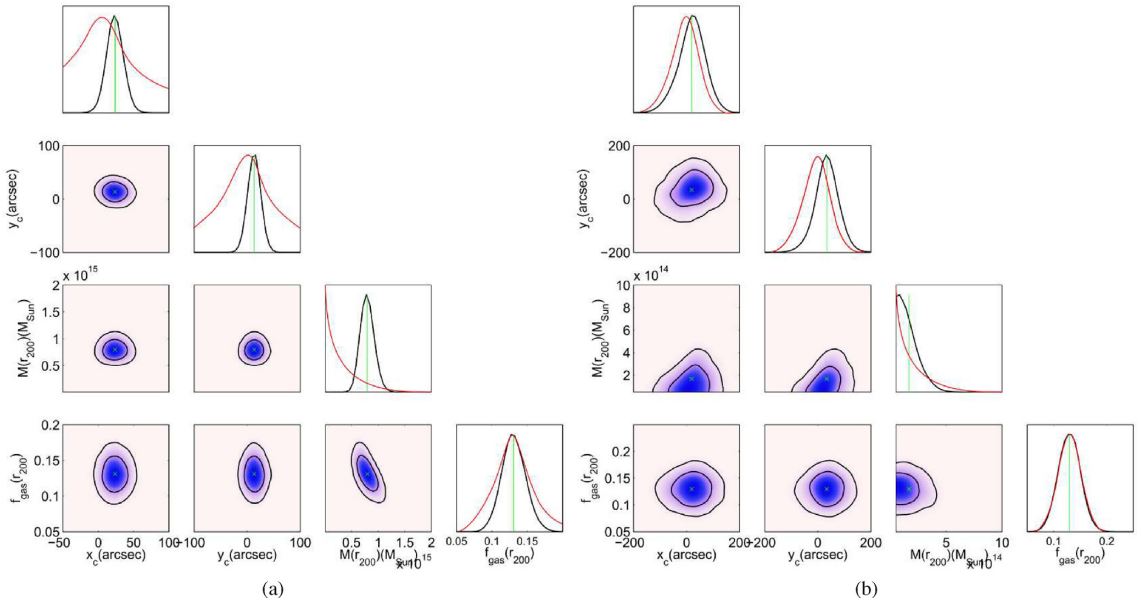

Figure 2. Posterior distributions derived from AMI data for the sampling parameters: $M(r_{200})$, $f_{\rm gas}(r_{200})$, $x_{\rm c}$, and $y_{\rm c}$. The contoured maps show the two-dimensional posteriors for the different pairs of parameters. The contours represent the 95 per cent and 68 per cent mean confidence intervals, with the green crosses denoting the expected value of the joint distributions. The four one-dimensional plots are the marginalized posteriors corresponding to the variable given at the bottom of the respective column. The red curves are the prior distributions on the respective parameters. Each green line is the expected value of the distribution. Posterior distributions in (a) show narrow distributions on the cluster mass, with the domain spanning feasible mass values for a galaxy cluster (cluster PSZ2 G184.68+28.91). In such cases the posteriors are said to be well constrained. The mass posteriors in (b) show that the data imply unphysical values for its mass, as the posterior distribution is hitting the lower bound of the prior (5×10^{13} M$\odot$) at almost its peak value (cluster PSZ2 G121.77+51.75). The distribution also resembles the uniform in log-space prior assigned to $M(r_{200})$. In such cases the posteriors are said to be poorly constrained with respect to the mass estimates.

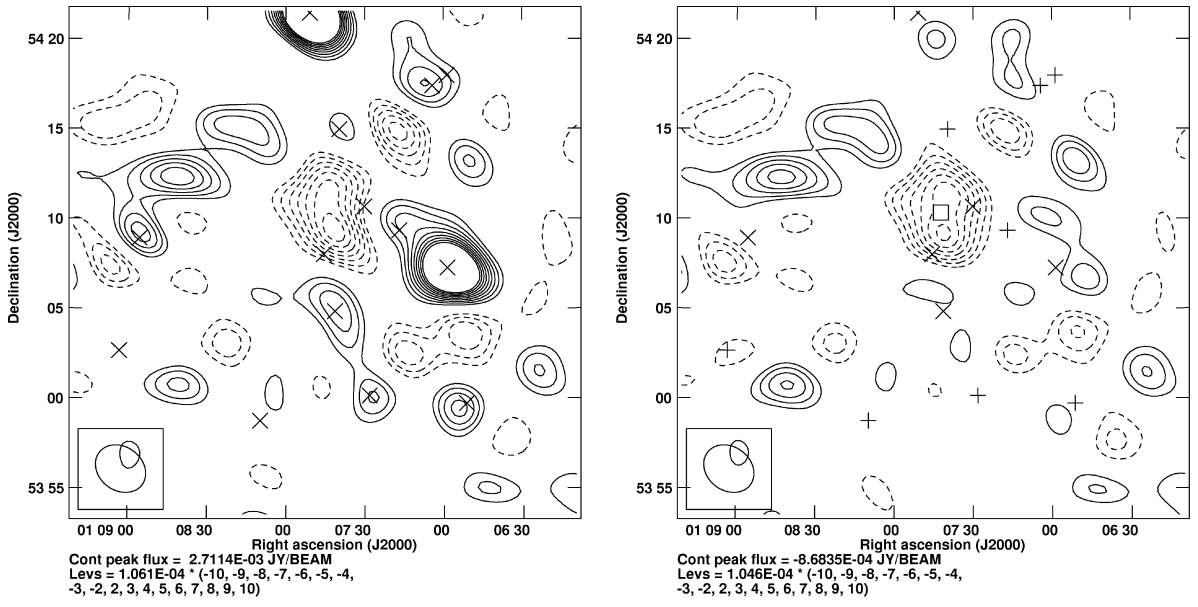

Figure 3. (a) Unsubtracted map produced from AMI observation of cluster PSZ2 G125.37−08.67. Contours are plotted at ±(2, 3, 4, ..., 10) × the rms noise level, and dashed contours are negative. (b) Source subtracted map produced from AMI observation for same cluster. The □ denotes the MCADAM-determined centre of the cluster (posterior mean values for $x_{\rm c}$ and $y_{\rm c}$). Here '+' signs denote radio-source positions as measured by the LA which were assigned delta priors on their parameters, whilst '×' denote sources which were assigned priors as described in Section 3.2.2.

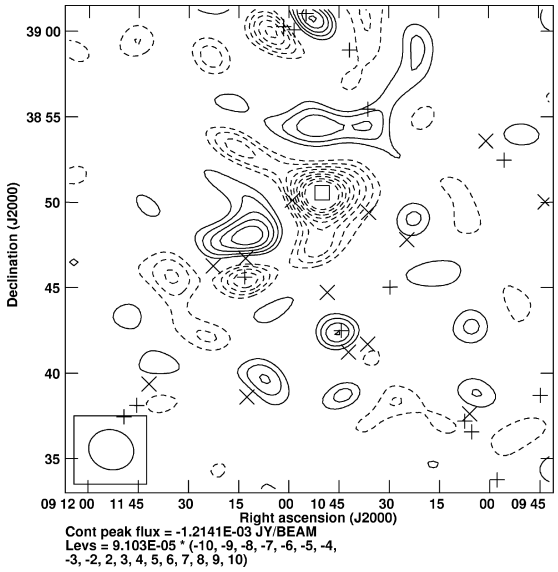

Figure 4. Subtracted map of cluster with ill-defined centre (cluster PSZ2 G183.90+42.99). The cluster is clearly offset from the observation pointing centre (middle of the map), and the lobes to the bottom and the top left of the cluster cause the centre position to be ambiguous.

only the clusters which showed good AMI posterior constraints means that clusters corresponding to a signal too faint for AMI to detect, clusters with large enough angular size for AMI's shortest baselines not to be able to measure the signal from the outskirts of the cluster ('resolved clusters'), and clusters where the radio-source and CMB contamination dwarfs the signal of the cluster, are all likely to have been excluded from the sample to some extent. In addition, removing the seven clusters with an ill defined centre likely removes some unrelaxed clusters from the sample.

4.2 AMI and PSZ2 mass estimates

The AMI and PSZ2 parameter estimates for the 54 clusters are given in Table 4. The clusters are listed in ascending order of z. Note that whether a redshift is photometric or spectroscopic is stated in the fifth column. All AMI values are the mean values of the corresponding parameter posterior distributions, with the error taken as the standard deviation. The estimates of the sampling parameters are included for comparison with each other, and with the sampling prior ranges and associated parameters given in Table 3. The AMI values for $M(r_{500})$ are given for comparison with the corresponding PSZ2 estimates. Two values for the PSZ2 mass estimates are given, $M_{\rm Pl,\,marg}(r_{500})$ and $M_{\rm Pl,\,slice}(r_{500})$. $M_{\rm Pl,\,marg}(r_{500})$ corresponds to the mass given by the $Y(r_{500})$–$M(r_{500})$ relation when the marginalized integrated Comptonization parameter is used as described in Section 3.3. The uncertainties associated with these Y values are taken as the standard deviations of the marginalized posteriors. $M_{\rm Pl,\,slice}(r_{500})$ is detailed in Section 3.3.2; its associated errors are calculated from the $Y(5r_{500})$ values where the slicing function intersects with the two ridges formed by the 68 per cent confidence interval values of the $Y(5r_{500})$ probability densities over the posterior domain of $\theta_{\rm p}$.

Fig. 5 shows $M(r_{200})$ as a function of z. Excluding the clusters at $z = 0.089$, 0.4, and 0.426, there is a steepening in mass between $0.1 \lessapprox z \lessapprox 0.5$ before it flattens off at higher z. This result is roughly consistent with the PSZ2 mass estimates (at r_{500}) obtained in Planck Collaboration XXVII (2016).

We now focus on the comparison between AMI and *Planck* mass estimates. Note that Planck Collaboration XXVII (2016) do not provide any means for estimating $M(r_{200})$ from their data, as r_{200} is the distance related to the scale radius ($r_{200} = c_{200} \times r_{\rm s}$) for the NFW dark matter profile given by equation (1), which they do not incorporate into their modelling process. Fig. 6 gives the AMI and two *Planck* estimates for $M(r_{500})$ versus the row number, in Table 4. We have not used z as the independent variable in this plot for clarity. The row number is monotonically related to z, as Table 4 is sorted by ascending z. From Fig. 6 it is clear that AMI underestimates the mass relative to both PSZ2 values. In fact $M(r_{500})$ is lower than $M_{\rm Pl,\,slice}(r_{500})$ in 37 out of 54 cases. $M(r_{500})$ is lower than $M_{\rm Pl,\,marg}(r_{500})$ in 45 out of 54 cases. 31 of the AMI masses are within one combined standard deviation of $M_{\rm Pl,\,slice}(r_{500})$, while 46 are within two. Four clusters have discrepancies larger than three combined standard deviations. Three of these clusters are at relatively low redshift ($\leq$0.25), whilst one is at $z = 0.43$.

Fig. 7 shows the pairwise ratios of mass estimates between the three different methods. The most obvious thing to note is that the ratio of PSZ2 masses is consistently greater than one, which again emphasizes the fact that the marginalization method attributes a much higher mass to the clusters than the slicing method. Furthermore, the ratio of AMI mass to the marginalized mass is small at medium redshift, which suggests that the marginalized mass is systematically high in this range. This graph also emphasizes that the AMI mass and the slicing methodology mass are the most consistent with one another.

5 AMI SIMULATIONS WITH PSZ2 MASS INPUTS

To investigate further the discrepancies between the mass estimates, it was decided to create simulated data based on the PSZ2 mass estimates obtained from the slicing methodology, which were then 'observed' by AMI. The data from these simulated observations were analysed the same way as the real data. The simulations were carried out using the in-house AMI simulation package PROFILE, which has been used in various forms in e.g. Grainge et al. (2002), Davies et al. (2011), Olamaie et al. (2012), and Olamaie et al. (2013). The input parameters for the simulation – which uses the physical model to create the cluster – are the sampling parameters of the model. Since Planck Collaboration XXVII (2016) do not give a method for calculating $M(r_{200})$ it was calculated as follows. First r_{500} was calculated by solving $M_{\rm SZ} = 500 \times \frac{4\pi}{3}\rho_{\rm crit}(z) r_{500}^3$ for r_{500}. r_{200} can be determined from r_{500}, but we note that the function mapping from r_{200} to r_{500} is non-invertible, thus r_{200} had to be calculated by solving equation (4) iteratively. $M(r_{200})$ can then be calculated from $M(r_{200}) = 200 \times \frac{4\pi}{3}\rho_{\rm crit}(z) r_{200}^3$.

As well as the values of $M(r_{200})$ derived from PSZ2 mass estimates, values for the other inputs were also required. We used $f_{\rm gas}(r_{200}) = 0.13$, $z = z_{\rm Planck}$, and $x_{\rm c} = y_{\rm c} = 0$ arcsec.

The objective of these simulations was to see whether we could recover the mass input into the simulation to create a cluster using the physical model, 'observed' by AMI and then analysed using the same model. We tried this for the four sets of simulations described below.

For each simulation different noise/canonical radio-source environment realizations (where relevant) were used each time. Due to the large sample size this should not affect any systematic trends seen in the results, and it avoids having to pick a particular realization to be used in all the simulations.

Table 4. Summary of values for final sample of 54 clusters. The redshift types correspond to S: spectroscopically measured and P: photometrically measured. z, $M(r_{200})$, x_c, y_c, and $f_{gas}(r_{200})$ are the physical model sampling parameters. $M_{AMI}(r_{500})$, $M_{Pl,\,marg}(r_{500})$, and $M_{Pl,\,slice}(r_{500})$ are the $M(r_{500})$ estimates obtained from the AMI and *Planck* data, respectively. All masses are given in units of $\times 10^{14}$ $M_\odot$ and all cluster centre coordinates are measured in arcseconds.

Row	*Planck* ID	Alias	z	z type	$M_{AMI}(r_{200})$	x_c	y_c	$f_{gas}(r_{200})$	$M_{AMI}(r_{500})$	$M_{Pl,\,marg}(r_{500})$	$M_{Pl,\,slice}(r_{500})$
1	PSZ2 G044.20+48.66	ACO2142	0.0894	S	13.49 ± 2.35	9.14 ± 18.20	8.80 ± 15.08	0.13 ± 0.02	9.25 ± 1.58	10.81 ± 0.42	$8.76\pm^{0.19}_{0.21}$
2	PSZ2 G053.53+59.52	ACO2034	0.113	S	8.51 ± 1.28	− 1.80 ± 13.10	19.39 ± 9.86	0.13 ± 0.02	5.87 ± 0.86	5.38 ± 0.39	$5.48\pm^{0.24}_{0.24}$
3	PSZ2 G151.90+11.63	CIZAJ0515.3+5845	0.12	S	5.74 ± 1.24	67.58 ± 27.09	68.01 ± 18.58	0.13 ± 0.02	3.99 ± 0.84	4.23 ± 1.03	$3.65\pm^{0.50}_{0.47}$
4	PSZ2 G218.59+71.31	ACO1272	0.137	S	2.70 ± 0.99	2.82 ± 25.21	−16.62 ± 25.98	0.13 ± 0.02	1.90 ± 0.68	4.79 ± 0.80	$3.62\pm^{0.30}_{0.30}$
5	PSZ2 G226.18+76.79	ACO1413	0.1427	S	8.19 ± 1.23	− 35.33 ± 10.98	−1.13 ± 13.44	0.13 ± 0.02	5.62 ± 0.82	6.14 ± 0.55	$5.98\pm^{0.25}_{0.25}$
6	PSZ2 G165.06+54.13	ACO990	0.144	S	7.80 ± 1.35	32.43 ± 13.21	−27.57 ± 15.52	0.14 ± 0.02	5.36 ± 0.90	5.13 ± 0.51	$4.83\pm^{0.28}_{0.29}$
7	PSZ2 G077.90−26.63	ACO2409	0.147	S	9.09 ± 1.32	− 26.87 ± 10.89	18.00 ± 11.85	0.14 ± 0.02	6.22 ± 0.88	5.92 ± 0.58	$5.08\pm^{0.27}_{0.27}$
8	PSZ2 G050.40+31.17	ACO2259	0.164	S	5.52 ± 1.19	35.72 ± 21.77	9.31 ± 19.56	0.13 ± 0.02	3.80 ± 0.80	4.53 ± 0.62	$4.36\pm^{0.35}_{0.36}$
9	PSZ2 G097.72+38.12	ACO2218	0.1709	S	10.65 ± 1.68	31.99 ± 15.25	−0.95 ± 13.52	0.13 ± 0.02	7.23 ± 1.11	7.44 ± 0.40	$6.64\pm^{0.17}_{0.17}$
10	PSZ2 G099.30+20.92	MCXCJ1935.3+6734	0.171	S	5.57 ± 1.24	− 37.19 ± 19.92	−24.50 ± 21.16	0.13 ± 0.02	3.83 ± 0.83	5.88 ± 0.93	$3.91\pm^{0.23}_{0.25}$
11	PSZ2 G067.17+67.46	ACO1914	0.1712	S	10.45 ± 1.49	31.39 ± 12.81	−33.15 ± 11.99	0.13 ± 0.02	7.09 ± 0.99	7.14 ± 0.47	$7.04\pm^{0.26}_{0.27}$
12	PSZ2 G167.67+17.63	RXJ0638.1+4747	0.174	S	4.78 ± 1.36	− 28.70 ± 31.24	10.76 ± 28.64	0.13 ± 0.02	3.30 ± 0.92	7.72 ± 0.81	$6.31\pm^{0.33}_{0.34}$
13	PSZ2 G066.68+68.44	ACO1902	0.181	S	4.95 ± 1.43	56.07 ± 25.47	8.14 ± 33.23	0.13 ± 0.02	3.41 ± 0.97	5.27 ± 0.84	$3.98\pm^{0.33}_{0.37}$
14	PSZ2 G065.28+44.53	ACO2187	0.183	S	5.24 ± 1.28	− 16.66 ± 22.61	−16.54 ± 21.65	0.13 ± 0.02	3.60 ± 0.86	3.89 ± 0.98	$3.56\pm^{0.47}_{0.51}$
15	PSZ2 G084.47+12.63	MCXCJ1948.3+5113	0.185	S	4.79 ± 1.22	− 73.73 ± 31.17	−16.97 ± 20.93	0.13 ± 0.02	3.30 ± 0.82	5.98 ± 0.65	$4.94\pm^{0.33}_{0.34}$
16	PSZ2 G100.04+23.73	ACO2317	0.21	S	5.44 ± 1.13	20.24 ± 19.02	−22.73 ± 20.90	0.13 ± 0.02	3.72 ± 0.75	4.10 ± 0.80	$3.73\pm^{0.29}_{0.31}$
17	PSZ2 G180.60+76.65	SDSSCGB26344.3	0.2138	S	5.38 ± 1.21	37.81 ± 15.59	−66.98 ± 19.41	0.13 ± 0.02	3.68 ± 0.81	6.76 ± 0.75	$6.00\pm^{0.35}_{0.34}$
18	PSZ2 G166.09+43.38	ACO773N	0.2172	S	9.84 ± 1.39	− 5.35 ± 10.66	−3.98 ± 9.70	0.13 ± 0.02	6.63 ± 0.92	7.76 ± 0.73	$6.87\pm^{0.34}_{0.32}$
19	PSZ2 G125.30−27.99	N/A	0.223	P	4.51 ± 1.31	− 8.08 ± 26.99	8.82 ± 30.24	0.13 ± 0.02	3.09 ± 0.87	5.54 ± 0.98	$4.70\pm^{0.56}_{0.55}$
20	PSZ2 G060.13+11.44	N/A	0.224	S	7.47 ± 1.22	− 64.79 ± 12.50	−49.27 ± 14.16	0.13 ± 0.02	5.06 ± 0.80	7.55 ± 1.09	$5.34\pm^{0.49}_{0.50}$
21	PSZ2 G166.62+42.13	ACO746	0.232	P	3.56 ± 1.07	− 38.98 ± 29.87	−38.09 ± 37.84	0.13 ± 0.02	2.44 ± 0.72	5.60 ± 0.71	$5.36\pm^{0.39}_{0.41}$
22	PSZ2 G097.94+19.43	4C 65.28	0.25	S	5.01 ± 1.31	− 114.76 ± 22.50	−13.64 ± 34.07	0.13 ± 0.02	3.40 ± 0.87	5.69 ± 0.85	$4.04\pm^{0.30}_{0.33}$
23	PSZ2 G164.29+08.94	N/A	0.251	P	5.97 ± 1.06	− 62.17 ± 14.03	18.12 ± 17.06	0.13 ± 0.02	4.04 ± 0.70	7.91 ± 1.36	$6.24\pm^{0.62}_{0.64}$
24	PSZ2 G133.60+69.04	RXJ1229.0+4737	0.254	S	5.26 ± 1.60	5.87 ± 25.04	59.40 ± 37.35	0.13 ± 0.02	3.57 ± 1.06	7.04 ± 0.97	$5.42\pm^{0.38}_{0.43}$
25	PSZ2 G086.47+15.31	MCXCJ1938.3+5409	0.26	S	10.89 ± 1.87	− 39.65 ± 13.24	19.83 ± 12.61	0.13 ± 0.02	7.25 ± 1.21	9.54 ± 0.63	$7.76\pm^{0.29}_{0.28}$
26	PSZ2 G139.62+24.18	N/A	0.2671	S	8.13 ± 1.28	36.66 ± 11.64	−12.58 ± 10.80	0.13 ± 0.02	5.45 ± 0.84	8.34 ± 1.06	$7.11\pm^{0.48}_{0.47}$
27	PSZ2 G184.68+28.91	ACO611	0.288	S	7.90 ± 1.02	22.61 ± 10.45	13.48 ± 9.97	0.13 ± 0.02	5.28 ± 0.67	11.44 ± 2.30	$5.61\pm^{0.52}_{0.53}$
28	PSZ2 G154.13+40.19	ACO747	0.29	P	6.46 ± 1.13	70.99 ± 14.72	−42.86 ± 13.25	0.13 ± 0.02	4.33 ± 0.74	6.09 ± 1.10	$5.48\pm^{0.45}_{0.46}$
29	PSZ2 G095.49+16.41	N/A	0.3	S	5.43 ± 1.12	− 24.47 ± 19.10	−102.18 ± 18.33	0.13 ± 0.02	3.65 ± 0.74	4.91 ± 0.99	$4.38\pm^{0.48}_{0.49}$
30	PSZ2 G109.52−19.16	N/A	0.3092	P	8.53 ± 1.40	− 30.38 ± 13.77	−15.21 ± 15.15	0.13 ± 0.02	5.66 ± 0.91	8.34 ± 1.79	$5.78\pm^{0.48}_{0.52}$
31	PSZ2 G198.90+18.16	[SPD2011] 298	0.3184	P	7.61 ± 1.18	26.76 ± 14.62	−58.07 ± 11.95	0.13 ± 0.02	5.06 ± 0.77	7.99 ± 1.47	$5.87\pm^{0.55}_{0.57}$
32	PSZ2 G152.33+81.28	MCXCJ1230.7+3439	0.333	S	6.27 ± 1.12	− 52.81 ± 20.78	44.11 ± 14.62	0.13 ± 0.02	4.17 ± 0.73	5.08 ± 0.96	$5.05\pm^{0.53}_{0.57}$
33	PSZ2 G108.17−11.56	N/A	0.336	S	8.00 ± 1.23	35.19 ± 13.14	−70.15 ± 19.09	0.13 ± 0.02	5.29 ± 0.80	9.82 ± 1.29	$7.42\pm^{0.57}_{0.60}$
34	PSZ2 G132.47−17.27	MCXCJ0142.9+4438	0.341	S	12.43 ± 1.85	31.87 ± 10.19	15.27 ± 12.93	0.13 ± 0.02	8.13 ± 1.18	8.27 ± 1.12	$8.07\pm^{0.61}_{0.65}$
35	PSZ2 G207.88+81.31	ACO1489	0.353	S	11.26 ± 1.61	68.55 ± 8.44	62.56 ± 11.55	0.13 ± 0.02	7.36 ± 1.02	8.01 ± 0.95	$7.54\pm^{0.45}_{0.45}$

Table 4 – *continued*

Row	*Planck* ID	Alias	z	z type	$M_{\rm AMI}(r_{200})$	$x_{\rm c}$	$y_{\rm c}$	$f_{\rm gas}(r_{200})$	$M_{\rm AMI}(r_{500})$	$M_{\rm Pl,\,marg}(r_{500})$	$M_{\rm Pl,\,slice}(r_{500})$
36	PSZ2 G157.32−26.77	MCSJ0308.9+2645	0.356	S	14.28 ± 2.12	0.33 ± 8.12	17.65 ± 11.53	0.13 ± 0.02	9.27 ± 1.34	10.95 ± 1.12	$10.67\pm^{0.64}_{0.65}$
37	PSZ2 G071.21 + 28.86	RXSJ175201.5+444046	0.366	S	9.26 ± 1.51	− 29.82 ± 9.95	−12.58 ± 13.26	0.13 ± 0.02	6.07 ± 0.96	6.15 ± 0.80	$6.70\pm^{0.44}_{0.46}$
38	PSZ2 G194.98+54.12	MCSJ1006.9+3200	0.375	P	8.90 ± 1.56	32.58 ± 12.17	−0.22 ± 19.18	0.13 ± 0.02	5.83 ± 1.00	6.31 ± 1.38	$5.30\pm^{0.65}_{0.68}$
39	PSZ2 G109.86+27.94	N/A	0.4	S	4.57 ± 1.28	3.98 ± 22.50	7.39 ± 18.70	0.13 ± 0.02	3.03 ± 0.83	5.23 ± 0.91	$5.23\pm^{0.45}_{0.48}$
40	PSZ2 G083.29−31.03	MCXCJ2228.6+2036	0.412	S	11.85 ± 1.73	81.05 ± 13.29	−3.42 ± 12.73	0.13 ± 0.02	7.65 ± 1.09	9.21 ± 0.95	$8.31\pm^{0.44}_{0.45}$
41	PSZ2 G063.38+53.44	NSCJ1537+392702	0.422	S	12.17 ± 1.94	46.13 ± 12.01	46.02 ± 9.37	0.13 ± 0.02	7.84 ± 1.22	7.78 ± 1.54	$6.17\pm^{0.58}_{0.62}$
42	PSZ2 G063.80+11.42	N/A	0.426	S	5.13 ± 1.19	− 36.41 ± 22.22	−47.14 ± 19.79	0.13 ± 0.02	3.37 ± 0.76	5.53 ± 0.63	$6.41\pm^{0.57}_{0.58}$
43	PSZ2 G157.43+30.34	RXJ0748.6+5940	0.45	P	11.64 ± 1.56	− 61.32 ± 7.38	4.53 ± 8.27	0.13 ± 0.02	7.47 ± 0.98	6.71 ± 0.44	$8.16\pm^{0.54}_{0.54}$
44	PSZ2 G150.56 + 58.32	CLGJ1115+5319	0.47	S	12.77 ± 2.40	10.18 ± 13.31	34.06 ± 18.57	0.13 ± 0.02	8.14 ± 1.49	10.04 ± 1.61	$7.44\pm^{0.50}_{0.53}$
45	PSZ2 G170.98+39.45	[SPD2011] 16774	0.5131	S	10.11 ± 1.38	31.48 ± 10.20	−30.87 ± 12.67	0.12 ± 0.02	6.43 ± 0.86	8.24 ± 1.30	$7.55\pm^{0.65}_{0.71}$
46	PSZ2 G094.56+51.03	N/A	0.5392	S	10.83 ± 1.43	81.61 ± 8.09	52.86 ± 8.80	0.13 ± 0.02	6.85 ± 0.88	6.46 ± 0.93	$5.90\pm^{0.45}_{0.44}$
47	PSZ2 G228.16+75.20	CLGJ1149+2223	0.545	S	15.63 ± 1.66	− 15.49 ± 5.32	17.11 ± 4.75	0.13 ± 0.01	9.78 ± 1.01	9.64 ± 0.94	$9.69\pm^{0.53}_{0.55}$
48	PSZ2 G213.39+80.59	SDSSCGB41791	0.5586	S	9.31 ± 1.32	− 9.73 ± 11.90	69.37 ± 12.14	0.13 ± 0.02	5.89 ± 0.81	8.03 ± 1.39	$6.77\pm^{0.63}_{0.65}$
49	PSZ2 G066.41+27.03	N/A	0.5699	S	13.23 ± 2.05	− 33.18 ± 11.12	97.03 ± 11.32	0.13 ± 0.02	8.27 ± 1.25	7.33 ± 0.82	$7.72\pm^{0.52}_{0.54}$
50	PSZ2 G144.83+25.11	CLGJ0647+7015	0.584	S	11.69 ± 1.46	4.15 ± 7.87	−1.21 ± 8.54	0.13 ± 0.02	7.32 ± 0.89	8.50 ± 1.27	$7.80\pm^{0.72}_{0.74}$
51	PSZ2 G045.87+57.70	N/A	0.611	S	9.22 ± 1.97	11.71 ± 14.87	24.21 ± 12.21	0.13 ± 0.02	5.78 ± 1.20	8.49 ± 1.61	$7.05\pm^{0.66}_{0.71}$
52	PSZ2 G108.27+48.66	N/A	0.674	S	9.31 ± 1.46	9.99 ± 11.34	35.79 ± 11.45	0.13 ± 0.02	5.77 ± 0.88	8.44 ± 1.58	$4.96\pm^{0.48}_{0.52}$
53	PSZ2 G086.93+53.18	N/A	0.6752	P	9.85 ± 1.69	− 47.72 ± 14.38	27.69 ± 10.67	0.13 ± 0.02	6.10 ± 1.01	6.07 ± 1.09	$5.46\pm^{0.51}_{0.52}$
54	PSZ2 G141.77+14.19	N/A	0.83	P	10.99 ± 1.50	− 4.36 ± 8.54	−19.02 ± 8.85	0.13 ± 0.02	6.61 ± 0.87	9.94 ± 2.01	$7.77\pm^{0.90}_{0.95}$

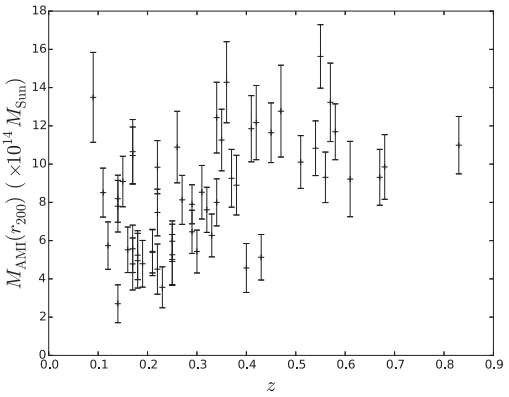

Figure 5. Plot of $M(r_{200})$ derived from AMI data using physical modelling verus redshift for the sample of 54 clusters.

5.1 Simulations of clusters plus instrumental noise

For each cluster, $M(r_{200})$ was calculated and Gaussian instrumental noise was added to the sky. The rms of the noise added was 0.7 Jy per channel per baseline per second, a value typical of an AMI cluster observation. Fig. 8 shows the map produced from the simulated data of cluster PSZ2 G044.20+48.66 plus this instrumental noise. The mass estimate derived from the Bayesian analysis of this cluster is 0.56 standard deviations above the input value.

Fig. 9 shows the difference between the input masses and the ones recovered from running the simulated observations through MCADAM, visualized using a histogram. All but three of the clusters lie within one standard deviation of the input mass, and even these clusters (PSZ2 G154.13+40.19, PSZ2 G207.88+81.31, and PSZ2 G213.39+80.59) give an output mass 1.01, 1.26, and 1.08 standard deviations below the input mass.

5.2 Simulations further adding confusion noise and primordial CMB

Confusion noise is defined to be the flux from radio-sources below a certain limit (here $S_{\rm conf} = 0.3$mJy). In this section all radio-source realizations only contribute to the confusion noise. However in Sections 5.3 and 5.4 sources above $S_{\rm conf}$ are included. The confusion noise contributions (see e.g. section 5.3 of FF09) were sampled from the probability density function corresponding to the 10C source counts given in Davies et al. (2011), and placed at positions chosen at random. Similarly, the primordial CMB realizations were sampled from an empirical distribution (Hinshaw et al. 2013), and randomly added to the maps.

Fig. 10 shows the map produced from the simulated data of cluster PSZ2 G044.20+48.66, including the three noise contributions. The mass estimate derived from the Bayesian analysis of this cluster is 0.22 standard deviations above the input value. The differences between output and input masses are shown in Fig. 11. This time

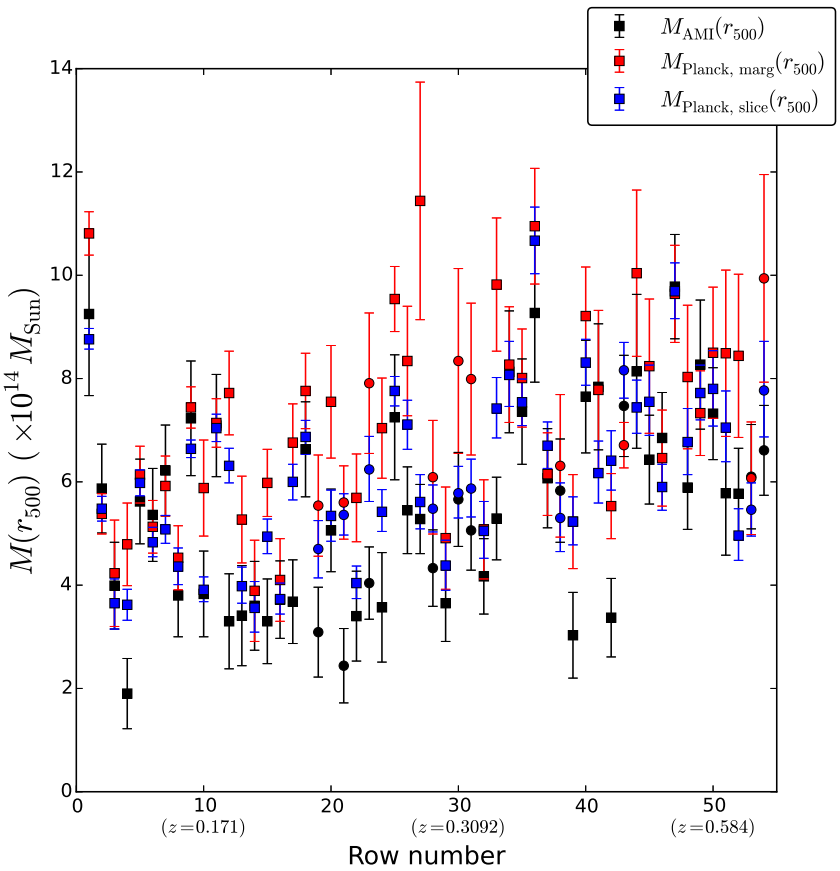

Figure 6. Plot of $M(r_{500})$ versus row number of Table 4 for three different cases: the value derived from AMI data using the physical model, $M_{\rm AMI}(r_{500})$; the value derived from *Planck* data using the marginalized value for $Y(5r_{500})$, $M_{\rm Pl,\ marg}(r_{500})$, and the value derived from *Planck* data using the slicing function value for $Y(5r_{500})$, $M_{\rm Pl,\ slice}(r_{500})$. The row number is monotonically related to z, as Table 4 is sorted by ascending z . The points with circular markers correspond to clusters whose redshifts were measured photometrically (as listed in Table 4).

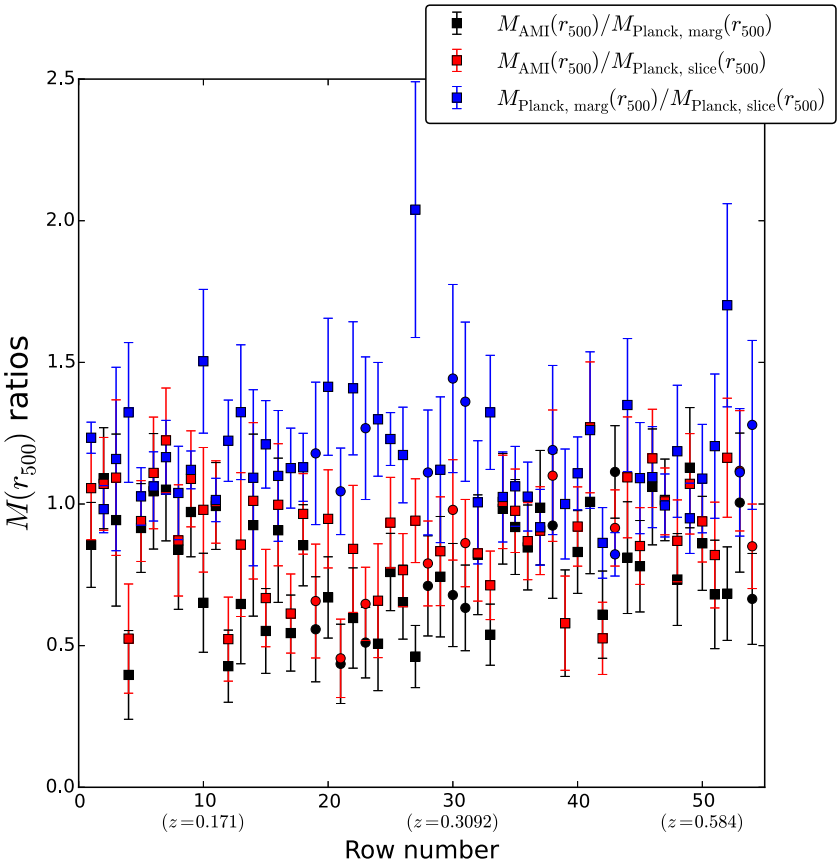

Figure 7. Plot of $M(r_{500})$ ratios versus row number of Table 4 for three different cases: $M_{\rm AMI}(r_{500})/M_{\rm Pl,\ marg}(r_{500})$, $M_{\rm AMI}(r_{500})/M_{\rm Pl,\ slice}(r_{500})$, and $M_{\rm Pl,\ marg}(r_{500})/M_{\rm Pl,\ slice}(r_{500})$. The points with square markers correspond to clusters whose redshifts were measured spectroscopically, and the circular markers correspond to photometric redshifts (as listed in Table 4).

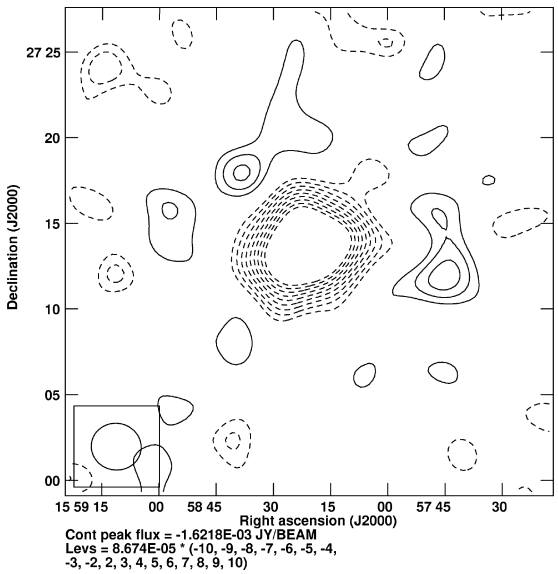

Figure 8. Unsubtracted map produced from simulated AMI data of cluster PSZ2 G044.20+48.66, including instrumental noise.

eight out of the 54 clusters cannot recover the input mass to within one standard deviation. In all eight of these cases, the mass is underestimated with respect to the input value. Five of the outlier values correspond to clusters at low redshift ($z < 0.2$).

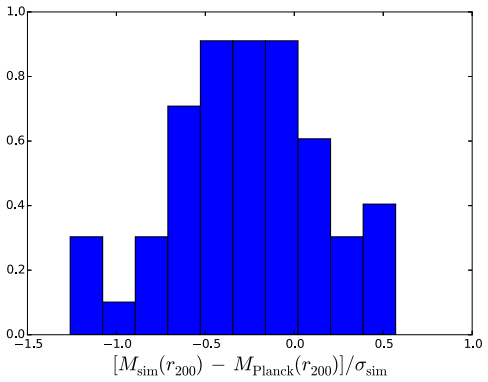

Figure 9. Normalized histogram of the differences between the input and output masses of the AMI simulations including the cluster and instrumental noise only, in units of standard deviations of the output mass.

5.3 Simulations further adding a canonical radio-source environment

The third set of simulations included recognized radio-sources, which formed a canonical radio-source environment. They were created in the same way as with the confusion noise described above, but with higher flux limits so that in reality, the LA would have been able to recognize them. The upper flux limit was set to 25 mJy.

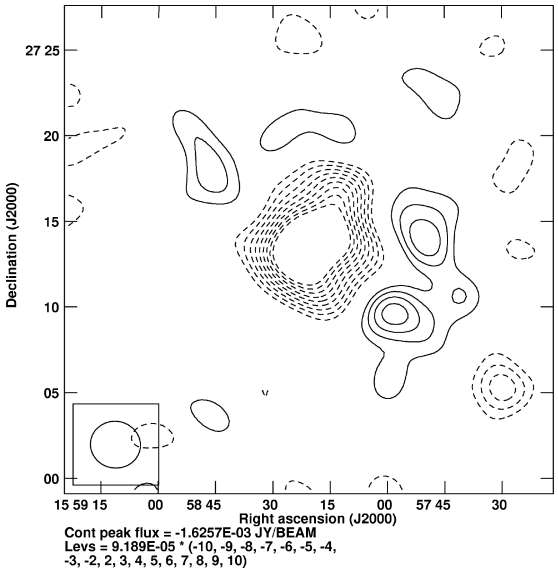

Figure 10. Unsubtracted map produced from simulated AMI data of cluster PSZ2 G044.20+48.66, including instrumental, confusion, and CMB noise.

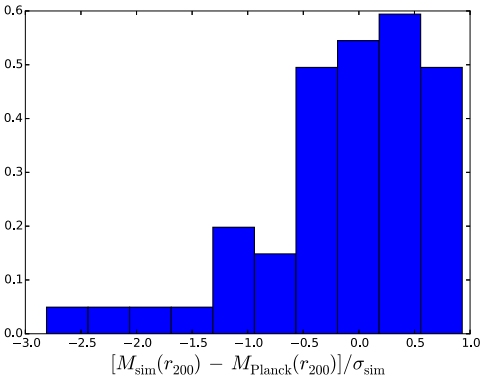

Figure 11. Normalized histogram of the differences between the input and output masses of the AMI simulations, in units of standard deviations of the output mass. This is the case for instrumental, confusion, and CMB noise contributions.

Fig. 12 shows the map produced from the simulated data of cluster PSZ2 G044.20+48.66, including a canonical source environment and background noise. The mass estimate derived from the Bayesian analysis of this cluster is 0.51 standard deviations below the input value. Fig. 13 shows that the canonical radio-source environment have little effect on the mass estimation relative to Section 5.2, as there are still eight clusters which give mass estimates greater than one standard deviation away from the input value. Note that in this case, the outliers occurred across the entire range of redshifts, which suggests that in Section 5.2 the low-redshift trend was just a coincidence.

5.4 Simulations with LA observed radio-source environment plus instrumental, confusion, and CMB noise

The final set of simulations included the radio-source environment measured by the LA during the real observation for each cluster. These are only estimates of the actual source environments, and are only as reliable as the LA's ability to measure them. Fig. 14 shows the maps produced from the real and simulated data of clus-

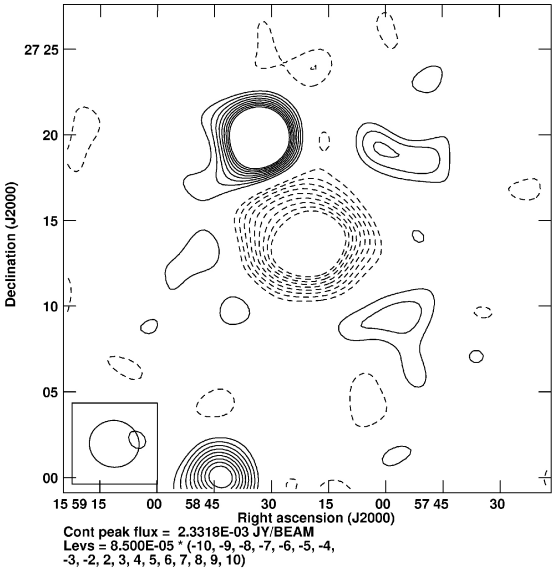

Figure 12. Unsubtracted map produced from simulated AMI data of cluster PSZ2 G044.20+48.66, including a canonical radio-source environment as well as instrumental, confusion, and CMB noise.

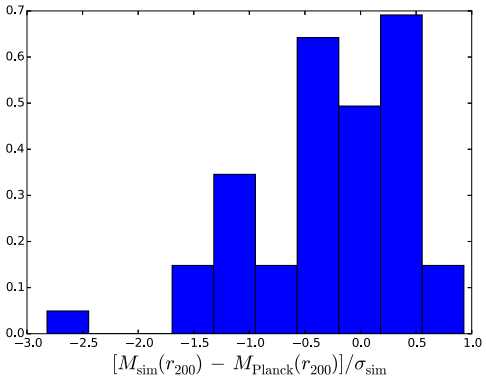

Figure 13. Normalized histogram of the differences between the input and output masses of the AMI simulations, in units of standard deviations of the output mass. This is the case for a canonical radio-source environment as well instrumental, confusion, and CMB noise contributions.

ter PSZ2 G044.20+48.66. The mass estimate derived from the Bayesian analysis of the simulated dataset is just 0.08 standard deviations above the input value.

Fig. 15 shows that including the LA observed radio-source environment has a large effect on the results, as this time there are 16 clusters which are more than one standard deviation away from the input mass. Furthermore, three of these overestimated the mass relative to the input, the first time we have seen this occur in any of the simulations. A possible source of bias could be due to for example, the empirical prior on the spectral index incorrectly modelling some radio-sources. Another source of bias could be the position of a source relative to the cluster, and the magnitude of the source flux. For example, if a high flux radio-source is close to the centre of the galaxy cluster, then even a slight discrepancy between the real and the modelled values for the source could have a large effect on the cluster parameter estimates.

We now compare these results to the simulations in YP15 (which concluded that the underestimation of the simulation input values could be due to deviation from the 'universal' profile, see figure 23a

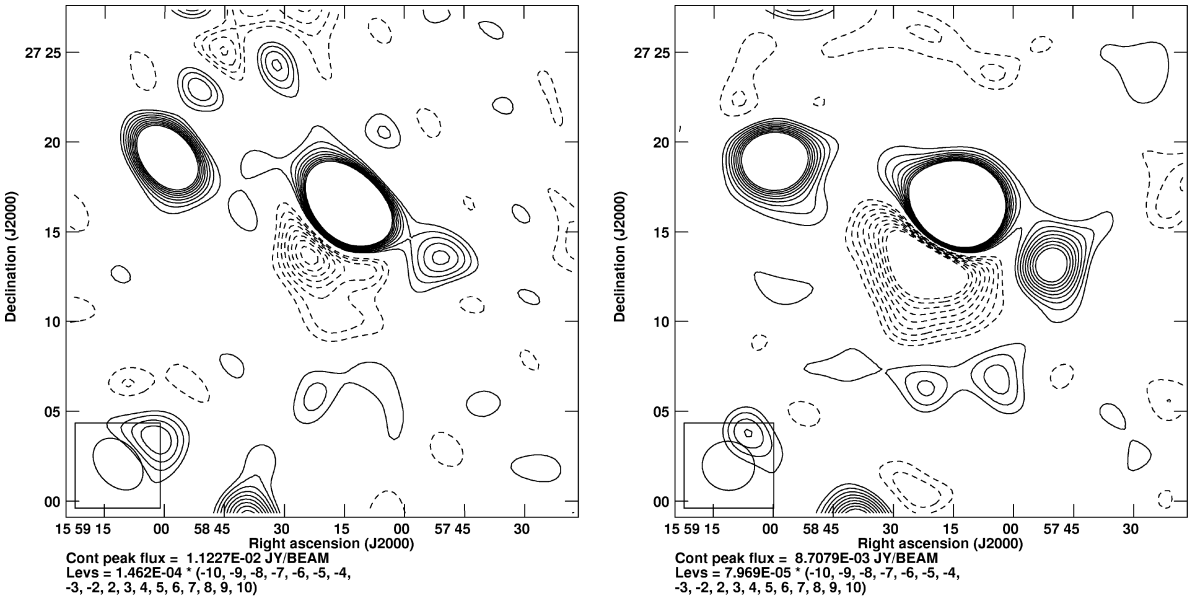

Figure 14. (a) Unsubtracted map produced from real AMI data of cluster PSZ2 G044.20+48.66. (b) Unsubtracted map produced from simulated AMI data of PSZ2 G044.20+48.66, including the real source environment (as measured by the LA) as well as instrumental, confusion, and CMB noise. The peak flux in the simulation has been underestimated relative to the real observation by ≈25 per cent. This could be due to the source sitting on a negative decrement caused by background noise, or it could be from the cluster decrement.

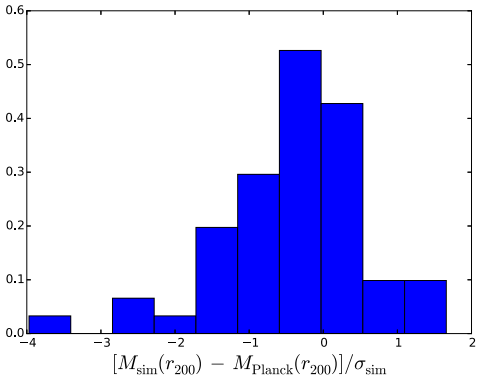

Figure 15. Normalized histogram of the differences between the input and output masses of the AMI simulations, in units of standard deviations of the output mass. This is the case for the real radio-source environment as measured by the LA, with instrumental, confusion, and CMB noise contributions.

in the paper). The results of the large cluster simulations (total integrated Comptonization parameter $= 7 \times 10^3$ arcmin^2 and $\theta_{\rm p} =$ 7.4 arcmin) in YP15 seem biased low at a more significant level than those in Fig. 15, as in the former case less than half of the clusters recover the true value within two standard deviations. For the smaller clusters however, YP15 found a slight upward bias in the simulation results, but this is probably smaller in magnitude than the bias found in this section.

5.5 Statistics of results of real and simulated data

Looking at the histograms produced in Sections 5.1, 5.2, 5.3, and 5.4, in the last three cases it is apparent that there is a negative skew in the data, i.e. the output masses are systematically low relative to the input masses. The skews calculated from the samples associated with the four histograms are −0.17, −1.30, −0.91, and −0.96, respectively, in units of standard deviations of the output mass. This suggests that the inclusion of confusion and CMB noise bias the AMI cluster mass estimates. We also calculate the median values associated with the histograms, and compare them with the medians corresponding to the real AMI and PSZ2 masses given in Fig. 6. The median values for the four histograms are −0.24, 0.09, −0.27, and −0.34, respectively, in units of standard deviations of the output mass. For the real data the median values for $(M_{\rm AMI}(r_{500})–M_{\rm Pl,\,marg}(r_{500}))/\sigma_{\rm AMI}$ and $(M_{\rm AMI}(r_{500})–M_{\rm Pl,\,slice}(r_{500}))/\sigma_{\rm AMI}$ are −1.57 and −0.56, respectively. It makes sense to compare the second of these real data values with those obtained from the simulations, as it was $M_{\rm Pl,\,slice}(r_{500})$ which was used to derive the input masses. The fact that the median from the real data is greater in magnitude than the values from the simulations implies in general, our simulations can recover their input values with better agreement than that obtained between real AMI estimates and those obtained from *Planck* data using the slicing function methodology. This seems plausible as you would expect that inferring results from data which were created using the same model used in the inference would be more accurate than results from data taken from two different telescopes, which use different models in their inference. Furthermore the simulation medians tell us that AMI is capable of inferring the masses derived with the slicing methodology, if the cluster is created using the model used in the inference and assuming there are no large discrepancies between the real and simulated AMI observations.

6 CONCLUSIONS

We have made observations of galaxy clusters detected by the *Planck* space telescope, with the AMI radio interferometer system in order to compare mass estimates obtained from their data. We then analysed this data using a physical model based on the

one described in Olamaie et al. (2012), following largely the data analysis method outlined in Feroz et al. (2009). This allowed us to derive physical parameter estimates for each cluster, in particular the total mass out to a given radius. We have also calculated two mass estimates for each cluster from *Planck*'s PowellSnakes detection algorithm (Carvalho et al. 2012) data following Planck Collaboration XXVII (2016) (PSZ2). We found the following:

(i) For the AMI mass estimates of *Planck* selected clusters there is generally a steeping in the mass of galaxy clusters as a function of redshift, which flattens out at around $z \approx 0.5$.

(ii) AMI $M(r_{500})$ estimates are within one combined standard deviation of the PSZ2 slicing function mass estimates for 31 out of the final sample of 54 clusters. However, the AMI masses are lower than both PSZ2 estimates for 37 out of the 54 cluster sample.

To investigate further the possible biasing of AMI mass estimates, we created simulations of AMI data with input mass values from the PSZ2 slicing methodology. We considered four different cases for the simulations: (1) galaxy cluster plus instrumental noise; (2) galaxy cluster plus instrumental plus confusion and CMB noise; (3) galaxy cluster plus instrumental, confusion, and CMB noise, plus a randomly positioned radio-source environment; (4) galaxy cluster plus instrumental, confusion, and CMB noise, plus the radio-source environment detected by the LA in the real observations. These simulated data sets were analysed in the same way as the real data sets, and we found the following:

(i) For case (1), the physical model recovered the input mass to within one standard deviation for 51 of the 54 clusters. The three which did not give an underestimate relative to the masses input to the simulation.

(ii) For case (2), eight of the simulations gave results which were more than one standard deviation lower than the input values. This highlights the effect of incorporating the noise sources into the error covariance matrix rather than trying to model the associated signals explicitly.

(iii) Case (3) shows similar results to case (2), which implies that 'ideal' radio-sources placed randomly in the sky have little effect on cluster mass estimates.

(iv) However in case (4) with real source environments, 16 simulations did not recover the input mass to within one standard deviation. This suggests that real radio-source environments, which can include sources with high-flux values, and often sources which are located very close to the cluster centre, introduce biases in the cluster mass estimates. In real observations there are also additional issues (the sources are not 'ideal'), such as sources being extended and emission not being circularly symmetric on the sky.

(v) Cases (2), (3) and (4) give distributions of output−input mass which are negatively skewed. Thus AMI mass estimates are expected to be systematically lower than the PSZ2 slicing methodology values.

(vi) Compared to the results of simulations of large clusters carried out in Perrott et al. (2015), which test the robustness of the 'universal' pressure profile, the case (4) bias appears relatively small in magnitude, and in the same direction (downward). When comparing the case (4) results with the small cluster simulations of Perrott et al. (2015), the latter shows a relatively small bias in the opposite direction.

(vii) The median values of the distributions of output−input mass of the simulations in each of the four cases are smaller in magnitude than those obtained from comparing AMI and PSZ2 estimates from real data. This is expected as we are using the same model to simulate and analyse the clusters in all four cases.

(viii) The simulated and real data medians also indicate that while the simulations have shown that AMI mass estimates are systematically low, this does not fully accommodate for the discrepancies in the results obtained from the real data. This suggests that there is a systematic difference between the AMI and *Planck* data and / or the cluster models used to determine the mass estimates (which generally leads to PSZ2 estimates being higher than those obtained from AMI data).

In a forthcoming paper (Javid et al. 2018), comparison of the 'observational' parameters (i.e. the integrated Comptonization parameter Y and the angular radius θ) obtained from AMI data will be analysed.

ACKNOWLEDGEMENTS

This work was performed using the Darwin Supercomputer of the University of Cambridge High Performance Computing (HPC) Service (http://www.hpc.cam.ac.uk/), provided by Dell Inc. using Strategic Research Infrastructure Funding from the Higher Education Funding Council for England and funding from the Science and Technology Facilities Council. The authors would like to thank Stuart Rankin from HPC and Greg Willatt and David Titterington from Cavendish Astrophysics for computing assistance. They would also like to thank Dave Green for his invaluable help using LaTeX. Kamran Javid acknowledges an STFC studentship. Yvette Perrott acknowledges support from a Trinity College Junior Research Fellowship.

REFERENCES

Arnaud M., Pratt G. W., Piffaretti R., Böhringer H., Croston J. H., Pointecouteau E., 2010, A&A, 517, A92
Bahcall J. N., Sarazin C. L., 1977, ApJ, 213, L99
Böhringer H. et al., 2007, A&A, 469, 363
Carvalho P., Rocha G., Hobson M. P., Lasenby A., 2012, MNRAS, 427, 1384
Chevallier M., Polarski D., 2001, IJMPD, 10, 213
Corless V. L., King L. J., Clowe D., 2009, MNRAS, 393, 1235
Davies J. I. et al., 2011, MNRAS, 415, 1883
Davies M. L. et al., 2011, MNRAS, 415, 2708
Feroz F., Hobson M. P., Zwart J. T. L., Saunders R. D. E., Grainge K. J. B., 2009, MNRAS, 398, 2049
Feroz F., Hobson M. P., Bridges M., 2009, MNRAS, 398, 1601
Franzen T. M. O. et al., 2011, MNRAS, 415, 2699
Gioia I. M., Maccacaro T., Schild R. E., Wolter A., Stocke J. T., Morris S. L., Henry J. P., 1990, ApJS, 72, 567
Grainge K., Jones M. E., Pooley G., Saunders R., Edge A., Grainger W. F., Kneissl R., 2002, MNRAS, 333, 318
Haehnelt M. G., Tegmark M., 1996, MNRAS, 279, 545
Hao J. et al., 2010, ApJS, 191, 254
Herranz D., Sanz J. L., Hobson M. P., Barreiro R. B., Diego J. M., Martínez-González E., Lasenby A. N., 2002, MNRAS, 336, 1057
Hickish J. et al., 2018, MNRAS, 475, 5677
Hinshaw G. et al., 2013, ApJS, 208, 19
Hobson M. P., Maisinger K., 2002, MNRAS, 334, 569
Hu W., Kravtsov A. V., 2003, ApJ, 584, 702
Javid K., Perrott Y. C., Hobson M. P., Olamaie M., Rumsey C., Saunders R. D. E., 2018, preprint (arXiv:1805.01968)
Komatsu E. et al., 2011, ApJS, 192, 18
Kravtsov A. V., Vikhlinin A., Nagai D., 2006, ApJ, 650, 128
Mehrtens N. et al., 2012, MNRAS, 423, 1024
Melin J.-B., Bartlett J. G., Delabrouille J., 2006, A&A, 459, 341

Nagai D., Kravtsov A. V., Vikhlinin A., 2007, ApJ, 668, 1
Navarro J. F., Frenk C. S., White S. D. M., 1995, MNRAS, 275, 720
Neto A. F. et al., 2007, MNRAS, 381, 1450
Olamaie M. et al., 2012, MNRAS, 421, 1136
Olamaie M., Hobson M. P., Grainge K. J. B., 2012, MNRAS, 423, 1534
Olamaie M., Hobson M. P., Grainge K. J. B., 2013, MNRAS, 430, 1344
Perley R. A., Butler B. J., 2013, ApJS, 204, 19
Perrott Y. C. et al., 2015, A&A, 580, A95
Petrov L., Kovalev Y. Y., Fomalont E. B., Gordon D., 2008, AJ, 136, 580
Piffaretti R., Arnaud M., Pratt G. W., Pointecouteau E., Melin J. B., 2011, A&A, 534, A109
Planck Collaboration III, 2013, A&A, 550, A129
Planck Collaboration VIII, 2011, A&A, 536, A8
Planck Collaboration IX, 2011, A&A, 536, A9
Planck Collaboration XI, 2011, A&A, 536, A11
Planck Collaboration XX, 2014, A&A, 571, A20
Planck Collaboration XXVI, 2015, A&A, 582, A29
Planck Collaboration XXVII, 2016, A&A, 594, A27
Planck Collaboration XXIX, 2014, A&A, 571, A29
Planck Collaboration XXXII, 2015, A&A, 581, A14
Planck Collaboration XXXVI, 2016, A&A, 586, A139
Rudy D. J., Muhleman D. O., Berge G. L., Jakosky B. M., Christensen P. R., 1987, Icarus, 71, 159
Rykoff E. S. et al., 2014, ApJ, 785, 104
Sunyaev R. A., Zeldovich Y. B., 1970, Comments Astrophys. Space Phys., 2, 66
Vikhlinin A., Kravtsov A., Forman W., Jones C., Markevitch M., Murray S. S., Van Speybroeck L., 2006, ApJ, 640, 691
Voges W. et al., 1999, A&A, 349, 389
Waldram E., Bolton R., Pooley G. G., Riley J. M., 2007, mru.conf, 140
Wechsler R. H., Bullock J. S., Primack J. R., Kravtsov A. V., Dekel A., 2001, preprint (astro-ph/0111069)
Wen Z. L., Han J. L., Liu F. S., 2012, ApJS, 199, 34
Willis J. P. et al., 2013, MNRAS, 430, 134
York D. G. et al., 2000, AJ, 120, 1579
Zwart J. T. L. et al., 2008, MNRAS, 391, 1545
Zwicky F., 1933, AcHPh, 6, 110
Zwicky F., 1937, ApJ, 86, 217

This paper has been typeset from a TEX/LATEX file prepared by the author.